Multi-Wave Coherent Control of a Solid State Single Emitter

F. Fras,[1,2,3,*] Q. Mermillod,[1,2] G. Nogues,[1,2] C. Hoarau,[1,2] C. Schneider,[4] M. Kamp,[4] S. Höfling,[4,5] W. Langbein,[6] and J. Kasprzak[1,2,†]

[1] *Univ. Grenoble Alpes, F-38000 Grenoble, France*
[2] *CNRS, Institut Néel, F-38000 Grenoble, France*
[3] *IPCMS UMR 7504, CNRS and Université de Strasbourg, Strasbourg, France*
[4] *Technische Physik and Wilhelm Conrad Röntgen Research Center for Complex Material Systems, Universität Würzburg, Germany*
[5] *SUPA, School of Physics and Astronomy, University of St Andrews, St Andrews, KY16 9SS, United Kingdom*
[6] *Cardiff University School of Physics and Astronomy, The Parade, Cardiff CF24 3AA, United Kingdom*

Coherent control of individual two-level systems (TLSs) is at the basis of any implementation of quantum information. An impressive level of control is now achieved using nuclear [1,2], vacancies [3,4] and charge spins [5,6]. Manipulation of bright exciton transitions in semiconductor quantum dots (QDs) is less advanced, principally due to the sub-nanosecond dephasing [7]. Conversely, owing to their robust coupling to light, one can apply tools of nonlinear spectroscopy [8] to achieve all-optical command. Here, we report on the coherent manipulation of an exciton via multi-wave mixing. Specifically, we employ three resonant pulses driving a single InAs QD. The first two induce a four-wave mixing (FWM) transient, which is projected onto a six-wave mixing (SWM) depending on the delay and area of the third pulse, in agreement with analytical predictions. Such a switch enables to demonstrate the generation of SWM on a single emitter and to engineer the spectro-temporal shape of the coherent response originating from a TLS. These results pave the way toward multipulse manipulations of solid state qubits via implementing the NMR-like control schemes [9] in the optical domain.

An appealing strategy to realize optically controlled quantum networks in solid state, is to coherently couple distant TLSs - like bright exciton transitions in QDs - via photons confined in microcavities [10,11] or propagating in waveguides [12–15]. The efficient retrieval and manipulation of coherent responses from single excitons is mandatory for assessing the properties of such solid state qubits and demonstrating the coherence transfer between them. In this context, substantial progress has been made by the introduction of the heterodyne spectral interferometry technique [8] to measure four-wave mixing (FWM) from individual excitons in various nanostructures [11,16–19]. Yet, measuring on single strongly-confined excitons in InAs QDs remains challenging and has not been previously achieved. This is due to their small dipole moment μ and the resulting required high resonant amplitudes of the three fields; $\mathcal{E}_1$, $\mathcal{E}_2$, $\mathcal{E}_3$, employed to drive the measured FWM polarization, being proportional to $\mu^4\mathcal{E}_1^*\mathcal{E}_2\mathcal{E}_3$ and higher order terms with the same phase dependence on the fields.

Here, the retrieval and manipulation of wave-mixing signals from single InAs QDs is accomplished by embedding them in a low-Q planar semiconductor microcavity [20], as detailed in Supplementary Fig. S2. Such a semiconductor hetero-structure provides an intracavity field enhancement of $\sqrt{Q} \simeq 13$ at the QDs position, whilst offering spectral matching of the photonic mode with femto-second laser pulses. This cavity-enhanced driving allows reducing the resonant excitation intensity, required to induce the FWM, by a factor around $Q^{3/2} \simeq 2200$. In consequence, the retrieval efficiency of wave-mixing signals from single excitons is improved by two orders of magnitude with respect to previous experiments on bare QDs [8,19]. In this work, we employ such wave-mixing responses to realize a novel scheme for ultrafast coherent control of optically active TLSs. We demonstrate gating of their coherent emission, by converting the FWM polarization into the SWM one. We show engineering of the FWM spectral response, also acting on the global spectral lineshape of a TLS. Details regarding the current experimental configuration are given in Supplementary Fig. S1.

For the purpose of the experiment described in this Letter, we require an optically active TLS in a solid. In InAs QDs, this is the case of negatively charged excitons (trions) [21], where the level structure can be trimmed down to two levels (disregarding spin degeneracy): the ground and excited states corresponding to the presence of an electron and a trion in the QD, respectively, as depicted in Fig. 1 a. We have therefore used a sample which is intentionally n-doped [20] with a Silicon δ-layer located in the cavity spacer. To illustrate the coherent response of trions, we present in Fig. 1 a the spectral interferogram detected at the FWM frequency $2\Omega_2 - \Omega_1$, as detailed in the Supplementary Material. Based on series of interferograms, we construct the FWM hyperspectral imaging [18], as exemplified in Fig. 1 b. Therein, the brightest, localized peaks correspond primarily to the FWM generated by trions. Such imaging is employed to determine spatial and spectral position of QDs. Also it enables a detailed statistical analysis on excitonic complexes, as exemplified for biexcitons in Supplementary Fig. S3.

We first retrieve the required parameters to infer and model the optical response of single emitters in a solid. The three-beam FWM spectroscopy offers direct access to coherence and population dynamics in the TLS. To probe the population dynamics, we detect the time-integrated FWM at the $\Omega_3 + \Omega_2 - \Omega_1$

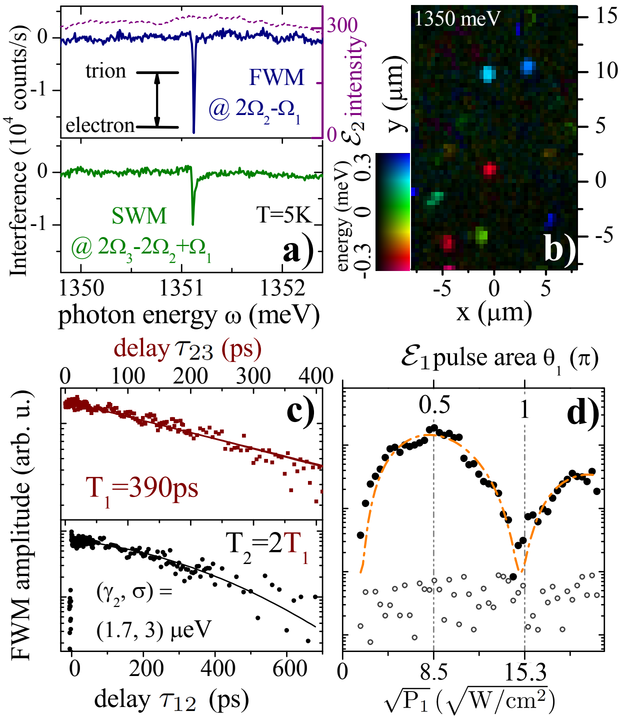

FIG. 1. **Wave mixing spectroscopy of individual negative trions in InAs QDs embedded in a low-Q microcavity.** a) Interferograms of four-wave mixing (FWM) of a single trion for $2\Omega_2 - \Omega_1$, $\tau_{12} = 0.5\,$ps and pulse areas $(\theta_1, \theta_2) = (\pi/2, \pi)$, and six-wave mixing (SWM) at $2\Omega_3 - 2\Omega_2 + \Omega_1$ for $\tau_{12} = 0.5\,$ps, $\tau_{23} = 1\,$ps, $(\theta_1, \theta_2, \theta_3) = (\pi/2, \pi, \pi)$. Integration time 20 s. Heterodyned spectral shape of $\mathcal{E}_2$ is shown with a purple, dashed line. b) Amplitude of the FWM hyperspectral imaging at $\tau_{12} = 1\,$ps. Localized peaks correspond to the FWM of single QDs: the amplitude is displayed as brightness, the energy is indicated as the hue of the colour range (indicated by the bar) from -0.3 (red) to +0.3 meV (blue) with respect to the chosen center of $\hbar\omega = 1350\,$meV. c) Population dynamics (brown squares) of the trion probed with FWM, $\tau_{12} = 0.5\,$ps: exponential decay (brown line) yields the population lifetime of $T_1 = (390 \pm 10)\,$ps. Coherence dynamics (black circles) of the same trion probed with FWM, consistent with radiatively limited dephasing T_2=2T_1 and a residual inhomogeneous broadening of $\sigma = (3 \pm 1)\,\mu$eV. d) FWM power as a function of $\sqrt{P_1} = |\mathcal{E}_1|$ and of $\mathcal{E}_1$ pulse area θ_1 showing Rabi oscillations, $\theta_2 = 2/3\pi$, $P_2 = |\mathcal{E}_2|^2 = 157\,\mathrm{W/cm}^2$, $\tau_{12} = 0.5\,$ps. Pulse areas of $(\theta_1, \theta_2) = (\pi/2, \pi)$, corresponding to $(P_1, P_2) = (72, 235)\,\mathrm{W/cm}^2$, are determined by the first maximum of the FWM versus θ_1 (θ_2, not shown). Predicted $\sin^2(\theta_1)\exp(-\xi\theta_1)$ is depicted by the orange dashed-dotted line, where ξ is the damping constant.

frequency, while varying the delay τ_{23} between $\mathcal{E}_2$ and $\mathcal{E}_3$ and fixing $\tau_{12} = 0.5\,$ps. The resulting evolution of the FWM amplitude is shown in Fig. 1 c and fitted by an exponential decay, yielding [22,23] the lifetime of $T_1 = (390 \pm 10)\,$ps. Conversely, detecting the FWM at the frequency $2\Omega_2 - \Omega_1$, reflects the coherence in the TLS. Its evolution is governed by the delay τ_{12} between $\mathcal{E}_1$ and $\mathcal{E}_2$, as displayed in Fig. 1 c. The lack of FWM at negative delays and the absence of fine-structure beating [19] confirm the trionic nature of the investigated transition. Our data are well described by the product of an exponential and a Gaussian decay [19]. From the former, we infer the dephasing time T_2 and the related homogenous broadening $\gamma_2 = 2\hbar/T_2$ (FWHM). The latter yields the inhomogeneous broadening σ due to the residual spectral wandering, occurring during the integration time. Note that even on the single transition level such wandering creates a photon echo, manifested here by a Gaussian decay of the coherence [19,24]. The coherence dynamics can be fitted using T_2=2T_1=780 ps and $\sigma = (3 \pm 1)\,\mu$eV. We thus find that the coherence of trions in these QDs approaches the radiative limit. This is supported by observation of their first order reflectance, as shown in Supplementary Fig. S5. More examples of such transitions close to the radiative limit are given in Supplementary Fig. S4.

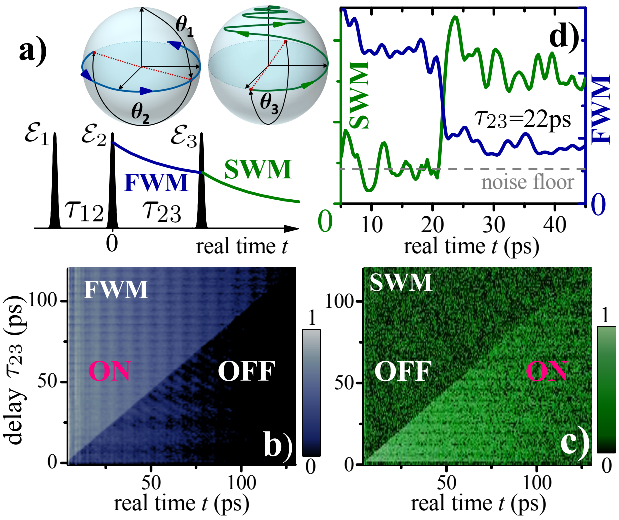

FIG. 2. **FWM/SWM switching.** a) Pulse sequence used in the experiment, highlighting rationale of the FWM/SWM switching. The evolution of the trion's Bloch vector (red) during FWM, switching and SWM is also depicted (ground state on the top of the sphere). The FWM transient (blue line) is created by $\mathcal{E}_1$ and $\mathcal{E}_2$ fields arriving at $t = -\tau_{12}$ and $t = 0$, respectively and it freely evolves during τ_{23}. $\mathcal{E}_3$, arriving at $t = \tau_{23}$, converts the FWM into the SWM (green line). The FWM/SWM conversion efficiency reaches unity for $\theta_3 = \pi$. FWM (b) and SWM (c) amplitudes as a function of real time t and delay τ_{23} for $\theta_3 = 0.8\pi$. FWM (SWM) signals are present above (below) the diagonal giving the arrival of $\mathcal{E}_3$. Amplitude on a linear colour scale, as given. Decreased amplitudes for long times is due to the limited resolution of the spectrometer. d) Demonstration of the FWM suppression (blue) and the SWM build up (green trace) at the arrival of $\mathcal{E}_3$ for $t = \tau_{23} = 22\,$ps. The noise floor is given by a gray dashed line. Note the coexistence of both signals for $t > 22\,$ps and corresponding residual signal in Fig. 3 c, owing to $\theta_3 \neq \pi$.

The coherent control experiment described below requires a calibration of the pulse areas $\theta_i = \int dt\, \mu|\mathcal{E}_i(t)|/\hbar$, which are proportional to the square root of the pulse intensities P_i. To illustrate this calibration, we present in Fig. 1 d the FWM power as a function of $\sqrt{P_1}$ and θ_1. As expected [16,25,26], the FWM undergoes Rabi oscillations with increasing θ_1. In addition, we observe a θ_1-dependent damping, which is attributed to dissipative coupling with acoustic phonons [27]. In the three-beam heterodyne spectral interferometry technique, the additional degree of freedom provided by the time delay τ_{23} allows to transform the FWM into SWM at the defined time after creating the FWM. Such SWM signals and their interferences with coexisting FWM have been studied in atomic physics [28,29]. Higher order wave-mixing has been also investigated in the condensed matter physics to explore many particle correlations in quantum wells [30–32] and QD ensembles [33], recently inferring their non-Markovian dynamics [34]. In the present study, we demonstrate for the first time generation of SWM on single emitters. Here, SWM detection serves as a tool to implement coherent control upon the FWM transient of a TLS. We use $\mathcal{E}_3$ pulse to project the FWM into the SWM signal oscillating at the $2\Omega_3 - 2\Omega_2 + \Omega_1$ frequency. The spectral interferogram measured at this frequency is shown in Fig. 1 a, for the applied pulse sequence given in Fig. 2 a. The FWM/SWM swapping is controlled by adjusting the pulse area θ_3 and τ_{23}, as derived in the analytical model presented in the Supplementary Material: FWM field $\mathcal{E}_{\boldsymbol{f}}$ and SWM field $\mathcal{E}_{\boldsymbol{s}}$ read:

$$|\mathcal{E}_{\boldsymbol{f}}(t)| \propto \sin\theta_1 \sin^2\frac{\theta_2}{2}\left(\Theta(t) - \sin^2\frac{\theta_3}{2}\Theta(t-\tau_{23})\right) \times e^{-t\gamma_2}, \tag{1}$$

$$|\mathcal{E}_{\boldsymbol{s}}(t)| \propto \sin\theta_1 \sin^2\frac{\theta_2}{2}\sin^2\frac{\theta_3}{2}\Theta(t-\tau_{23})e^{-t\gamma_2}, \tag{2}$$

where Θ is the Heaviside function, and $t = 0$ is defined by the arrival of $\mathcal{E}_2$.

Conversion of FWM into SWM and their coexistence is experimentally demonstrated in Fig. 2. Therein, we present the FWM and SWM field amplitude transients for increasing τ_{23} at $\theta_3 = 0.8\pi$. In such maps, the arrival of $\mathcal{E}_3$ at $t = \tau_{23}$, generating the conversion, defines the diagonal. From Eqs. (1) and (2), we expect that the FWM is present in the upper-side of the diagonal ($t < \tau_{23}$), and has been converted to SWM in the lower-side ($t > \tau_{23}$), as indeed measured. This temporal gating of both signals is the key to manipulate the spectral distribution of the FWM from a TLS.

We note that the conversion efficiency reaches unity for the $\theta_3 = \pi$ yielding, at the arrival of $\mathcal{E}_3$, a complete suppression of the FWM. In Fig. 3, we employ specific pulse areas $(\theta_1, \theta_2) = (\frac{\pi}{2}, \pi)$ in order to drive, between $\mathcal{E}_2$ and $\mathcal{E}_3$, the maximum polarization to the FWM, consistent with Eq. (1). In Fig. 3 a we present FWM transients measured at $\theta_3 = \pi$ for various τ_{23}. Their spectral amplitudes (also see Supplementary Fig. S6) are given in Fig. 3 b. The spectra show a substantial broadening and ringing due to the step-like suppression in time, leading to a sine cardinal like shape. FWM at $\theta_3 = 0$ (topmost) is given for comparison. The effect, also clearly visible in Fig. 3 c, is observable from $\tau_{23} = 110$ ps to $\tau_{23} = 10$ ps where the FWHM of the main peak increases from 38 μeV (given by the spectral resolution) up to 700 μeV. This represents an imposed broadening by two orders of magnitude with respect to γ_2. With further decrease of τ_{23} such spectral broadening can reach 10 meV range, as is only bounded by the duration of $\mathcal{E}_3$. Due to the limited amount of the emitted FWM for $\tau_{23} \simeq 0$, its observation requires a large signal-to-noise ratio. Fourier transforming Eq. (1) with respect to the real time t, yields the spectrally resolved FWM amplitude:

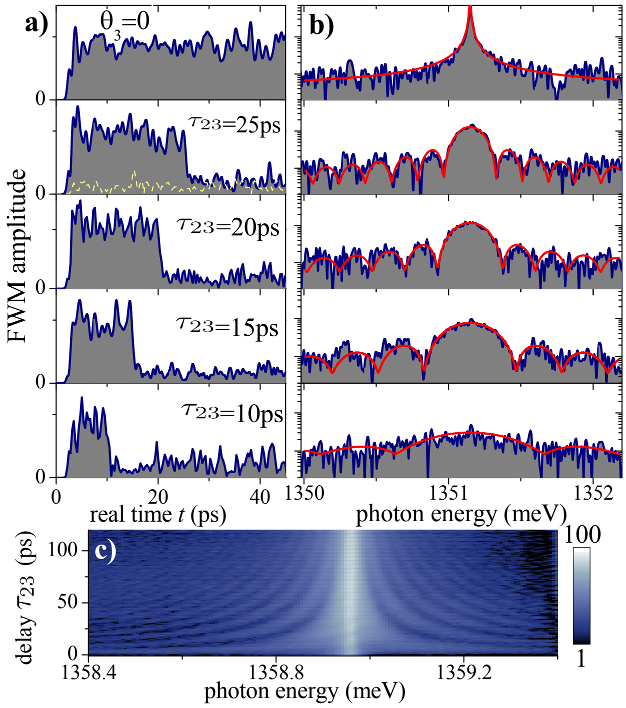

FIG. 3. **Manipulation of the coherent response of a single emitter via wave-mixing switching.** a) FWM transients generated for $\tau_{12} = 0.2$ ps, $\theta_3 = \pi$ and τ_{23} as labeled. A complete suppression of the FWM is observed after the arrival of $\mathcal{E}_3$ ($t > \tau_{23}$); the noise level is shown by the dashed yellow line. The free evolution of the FWM for $\theta_3 = 0$ is shown in the topmost panel. b) FWM spectral amplitudes of the data in a), showing a substantial spectral broadening of the FWM due to the step-like suppression of the signal in time domain. Analytical predictions using Eq. (3) are shown as red lines. c) FWM spectral amplitudes of the transients given in Fig. 2 b, showing the evolution of the FWM lineshape with increasing τ_{23} for $\theta_3 = 0.8\pi$. Logarithmic colour scale, as shown by the vertical bar.

$$|\mathcal{E}_{\boldsymbol{f}}(\omega)| \propto \sin\theta_1 \sin^2\frac{\theta_2}{2} e^{-\tau_{12}\gamma_2} \times \left(\frac{1 + \sin^4\frac{\theta_3}{2}e^{-2\tau_{23}\gamma_2} - 2\sin^2\frac{\theta_3}{2}e^{-\tau_{23}\gamma_2}\cos\Delta\omega\tau_{23}}{2\pi(\gamma_2^2 + \Delta\omega^2)}\right)^{1/2} \tag{3}$$

where $\Delta\omega = \omega - \omega_{eg}$. With the particular pulse areas $(\theta_1, \theta_2, \theta_3) = (\frac{\pi}{2}, \pi, \pi)$, the spectrum takes the simple form $e^{-\gamma_2(\tau_{12}+\tau_{23})}\left(\frac{\cosh(\gamma_2\tau_{23}) - \cos(\Delta\omega\tau_{23})}{\pi(\gamma_2^2+\Delta\omega^2)}\right)^{1/2}$, which reproduces the observed features quantitatively, as shown by red traces in Fig. 3 b. The spectral broadening of the central peak scales as $\frac{2\pi\hbar}{\tau_{23}}$, characteristic of the sine cardinal lineshape.

For intermediate values of θ_3, the FWM is only partially converted to SWM. Therefore both non-linearities coexist, as can be noted in Fig. 2 d. This is investigated in Fig. 4, where the FWM transients (a)

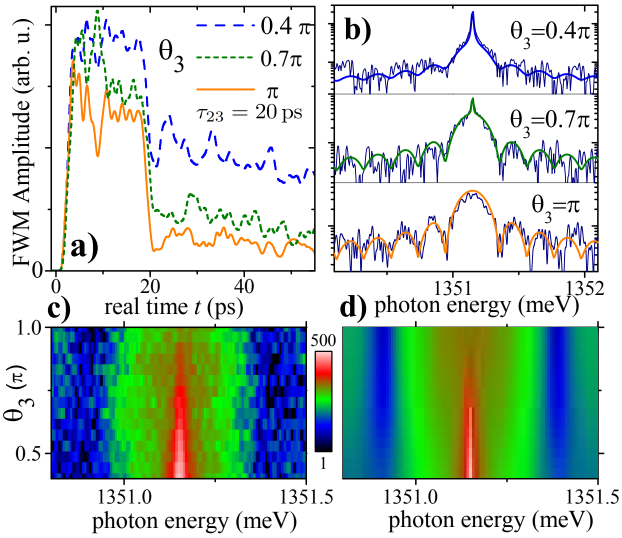

FIG. 4. **Manipulation of the FWM with the area of the control pulse $\mathcal{E}_3$.** a) Measured evolution of the FWM transient for θ_3 of 0.4π (blue dashed), 0.7π (green dotted) and π (orange solid); for $\tau_{12} = 0.2$ ps and $\tau_{23} = 20$ ps. An increasing suppression of the FWM for $t > \tau_{23}$ with increasing θ_3 is observed. b) FWM spectral amplitudes of the transients shown in a), with the corresponding theoretical prediction according to Eq. (3). c) Map of the FWM spectral amplitude as a function of θ_3 demonstrating a gradual suppression of the spectrally narrow component of the FWM. Delays as in a). d) Theoretical simulation of c). Logarithmic color scale, as shown with the colour bar.

and spectra (b) for increasing θ_3 and fixed $\tau_{23} = 20$ ps are presented. Owing to the increasing FWM suppression for $t > 20$ ps, the amplitude of the spectrally narrow component is reduced (see Supplementary Fig. S7). In parallel, the broad pedestal develops. Hence, non-natural lineshapes can be designed by tuning θ_3 and τ_{23}. Eq. (3), derived in the Supplementary Material, reproduces the experimental data shown in Fig. 4 b and c, without any free parameters, apart from the absolute common scaling.

The ability to manipulate the spectral width of a coherent response from the TLS provides a novel degree of freedom in solid state quantum optics. We emphasize that the phase shift induced by the FWM/SWM conversion modifies the coherent oscillation of the dipole: the global lineshape of the TLS polarization is altered, as highlighted in Supplementary Fig. S8. The latter is strikingly manifested when the $\mathcal{E}_3$ is heterodyned at $2\Omega_2 - \Omega_1$, leading to a stationary phase shift between the two non-linearities generated by $\mathcal{E}_2$ and $\mathcal{E}_3$, respectively. Therefore by adjusting this phase shift with τ_{23} (see Eqs. (11) and (12) in the Supplementary Material), we can perform controlled phase rotations of the TLS dipole. After arrival of $\mathcal{E}_3$, the phase of the TLS emission could be inverted or entirely frozen. Such on-demand blockade of emission represents a fundamental step in optical control of single TLS systems. As an example of application, let us note that tuning the spectral shape of a TLS could be employed to optimize injection and storing of single photons in optical resonators. Furthermore, maximizing the spectral overlap within a pair of distant TLSs promotes their coherent coupling via propagating photons [35], which is a prerequisite to realize optically controlled quantum networks in a solid. Multiwave mixing could be also used to selectively address the coherence dynamics and transitions in higher manifolds of the Jaynes-Cummings ladder of nanophotonic devices operating in a strong-coupling regime [11,17].

By employing a low-Q semiconductor microcavity, we improved the retrieval sensitivity of coherent responses from individual emitters, enabling wave mixing spectroscopy of individual excitons in strongly-confined InAs QDs. Using three beam configuration, we inferred a new scheme for controlling coherent evolution of a TLS via converting FWM to SWM. We have demonstrated that, via temporal gating of the FWM, we can control its lineshape by varying the amplitude and the arrival time of the gate pulse. The demonstration of SWM on individual emitters paves the way towards investigations of their non-Markovian dynamics [34] and to study higher order correlations [30] involving more than two excitons within a QD. Extending our proof-of-principle protocol toward control via multi-wave mixing is conceptually straightforward: conversion between wave mixing processes is determined by areas and respective delays of driving pulses. It is also technically feasible via multiplexed digital heterodyning. An alluring perspective is to perform multi-wave mixing on radiatively coupled pairs of distant excitons [35], achieving non-local quantum control in a solid.

We acknowledge support by the European Research Council Starting Grant "PICSEN" contract no. 306387.

---

[*] francois.fras@ipcms.unistra.fr
[†] jacek.kasprzak@neel.cnrs.fr
[1] Pla, J. J. *et al.* High-fidelity readout and control of a nuclear spin qubit in silicon. *Nature* **496**, 334–338 (2013).
[2] Muhonen, J. T. *et al.* Storing quantum information for 30 seconds in a nanoelectronic device. *Nat. Nanotechnol.* **9**, 986–991 (2014).
[3] Widmann, M. *et al.* Coherent control of single spins in silicon carbide at room temperature. *Nature Mater.* **14**, 164–168 (2015).
[4] Yale, C. G. *et al.* All-optical control of a solid-state spin using coherent dark states. *Proc. Natl. Acad. Sci. U.S.A* **110**, 7595–7600 (2013).
[5] Carter, S. G. *et al.* Quantum control of a spin qubit coupled to a photonic crystal cavity. *Nature Photon.* **7**, 329–334 (2013).
[6] Hansom, J. *et al.* Environment-assisted quantum control of a solid-state spin via coherent dark states. *Nature Phys.* **10**, 725–730 (2014).
[7] Borri, P. *et al.* Ultralong dephasing time in InGaAs quantum dots. *Phys. Rev. Lett.* **87**, 157401 (2001).

[8] Langbein, W. & Patton, B. Heterodyne spectral interferometry for multidimensional nonlinear spectroscopy of individual quantum systems. *Opt. Lett.* **31**, 1151 (2006).
[9] Vandersypen, L. M. K. & Chuang, I. L. NMR techniques for quantum control and computation. *Rev. Mod. Phys.* **76**, 1037 (2005).
[10] Reithmaier, J. P. *et al.* Strong coupling in a single quantum dot-semiconductor microcavity system. *Nature* **432**, 197–200 (2004).
[11] Albert, F. *et al.* Microcavity controlled coupling of excitonic qubits. *Nature Comm.* **4**, 1747 (2013).
[12] Luxmoore, I. J. *et al.* Interfacing spins in an InGaAs quantum dot to a semiconductor waveguide circuit using emitted photons. *Phys. Rev. Lett.* **110**, 037402 (2013).
[13] Coles, R. J. *et al.* Waveguide-coupled photonic crystal cavity for quantum dot spin readout. *Opt. Express* **22**, 2376–2385 (2014).
[14] Reichert, T. *et al.* Highly directed emission from self-assembled quantum dots into guided modes in disordered photonic-crystal waveguides. *Phys. Rev. B* **90**, 115310 (2014).
[15] Arcari, M. *et al.* Near-unity coupling efficiency of a quantum emitter to a photonic crystal waveguide. *Phys. Rev. Lett.* **113**, 093603 (2014).
[16] Patton, B., Woggon, U. & Langbein, W. Coherent control and polarization readout of individual excitonic states. *Phys. Rev. Lett.* **95**, 266401 (2005).
[17] Kasprzak, J. *et al.* Up on the Jaynes-Cummings ladder of a quantum-dot/microcavity system. *Nat. Mater.* **9**, 304–308 (2010).
[18] Kasprzak, J., Patton, B., Savona, V. & Langbein, W. Coherent coupling between distant excitons revealed by two-dimensional nonlinear hyperspectral imaging. *Nat. Phot.* **5**, 123 (2011).
[19] Kasprzak, J. *et al.* Vectorial nonlinear coherent response of a strongly confined exciton-biexciton system. *New J. Phys.* **15**, 055006 (2013).
[20] Maier, S. *et al.* Bright single photon source based on self-aligned quantum dot-cavity systems. *Optics Ex.* **22**, 8136 (2014).
[21] Benny, Y. *et al.* Excitation spectroscopy of single quantum dots at tunable positive, neutral, and negative charge states. *Phys. Rev. B* **86**, 085306 (2012).
[22] Langbein, W. *et al.* Radiatively limited dephasing in InAs quantum dots. *Phys. Rev. B* **70**, 033301 (2004).
[23] Proux, R. *et al.* Measuring the photon coalescence time window in the continuous-wave regime for resonantly driven semiconductor quantum dots. *Phys. Rev. Lett.* **114**, 067401 (2015).
[24] Patton, B., Langbein, W., Woggon, U., Maingault, L. & Mariette, H. Time- and spectrally-resolved four-wave mixing in single CdTe/ZnTe quantum dots. *Phys. Rev. B* **73**, 235354 (2006).
[25] Bonadeo, N. H. *et al.* Coherent optical control of the quantum state of a single quantum dot. *Science* **282**, 1473 (1998).
[26] Stievater, T. H. *et al.* Rabi oscillations of excitons in single quantum dots. *Phys. Rev. Lett.* **87**, 133603 (2001).
[27] Ramsay, A. *et al.* Phonon-induced Rabi-frequency renormalization of optically driven single InGaAs/GaAs quantum dots. *Phys. Rev. Lett.* **105**, 177402 (2010).
[28] Zhang, Y., Brown, A. W. & Xiao, M. Observation of interference between four-wave mixing and six-wave mixing. *Optics Lett.* **32**, 1120 (2007).
[29] Zhang, Y., Khadka, U., Anderson, B. & Xiao, M. Temporal and spatial interference between four-wave mixing and six-wave mixing channels. *Phys. Rev. Lett.* **102**, 013601 (2009).
[30] Turner, D. & Nelson, K. Coherent measurements of high-order electronic correlations in quantum wells. *Nature* **466**, 1089–1092 (2010).
[31] Axt, V. M., Bolton, S. R., Neukirch, U., Sham, L. J. & Chemla, D. S. Evidence of six-particle coulomb correlations in six-wave-mixing signals from a semiconductor quantum well. *Phys. Rev. B* **63**, 115303 (2001).
[32] Voss, T. *et al.* Biexcitonic effects in the coherent control of the excitonic polarization detected in six-wave-mixing signals. *Phys. Rev. B* **66**, 155301 (2002).
[33] Moody, G. *et al.* Fifth-order nonlinear optical response of excitonic states in an InAs quantum dot ensemble measured with two-dimensional spectroscopy. *Phys. Rev. B* **87**, 045313 (2013).
[34] Tahara, H., Ogawa, Y., Minami, F., Akahane, K. & Sasaki, M. Long-time correlation in non-markovian dephasing of an exciton-phonon system in InAs quantum dots. *Phys. Rev. Lett.* **112**, 147404 (2014).
[35] Minkov, M. & Savona, V. Radiative coupling of quantum dots in photonic crystal structures. *Phys. Rev. B* **87**, 125306 (2013).